

Magnitude and phase reciprocity calibration of ultrasonic piezoelectric disk in air

Kenneth K. Andersen^{1,3}, Per Lunde^{1,2}, Jan Kocbach²

¹ University of Bergen, Dept. of Physics and Technology, PB 7803, NO-5020 BERGEN, Norway

² Christian Michelsen Research AS, PB 6031 Postterminalen, NO-5892 BERGEN, Norway

³ University College of Southeast Norway, PB 235, 3603 Kongsberg, Norway

Contact email: kenneth.andersen@hbv.no

Abstract

A modified conventional three-transducer reciprocity calibration method is used to measure the magnitude and phase responses of the transmitting voltage response and the free-field open-circuit receiving voltage sensitivity of ultrasonic piezoelectric transducers radiating in air at 1 atm. The transducers used in this work are 20 x 2 mm circular piezoelectric ceramic disks with their first and second radial modes at approximately 100 and 250 kHz, respectively. The transducer characterization is supported and aided by finite element simulations of the measurement system and the measured frequency responses. Preliminary results indicate that the magnitude and phase responses of the transmitting voltage response and the free-field open-circuit receiving voltage sensitivity can be measured with fair accuracy in a limited frequency band around the first radial mode of the piezoelectric ceramic disk. Further work is needed to demonstrate and quantify the accuracy actually obtained using the three-transducer reciprocity calibration method, to achieve transducer characterization at a calibration accuracy level, and to achieve calibration above the calibrated frequency range of the B&K 4138 microphone.

1 Introduction

Ultrasonic measurement technologies are used in a wide range of application areas and industries, from petroleum and marine applications, to medicine. For gas applications, such as fiscal measurement [1–3], quality, and energy measurement of natural gas [4–6], accurate calibration data for ultrasonic transducers may be important to frequencies of 300 kHz and higher.

A range of calibration methods are available for transducers in gas or liquid [7–25]. In gas, challenges concerning these calibration techniques arise for frequencies exceeding approximately 150 kHz. For instance, for the 1/8 inch B&K 4138 condenser microphone, accurate calibration data are available from the manufacturer up to 140 kHz [26, 27].

The present work addresses characterization of transducers for use in gas at ultrasonic frequencies, as a contribution in the long-time perspective to achieve accurate magnitude and phase characterization at these frequencies, possibly at calibration accuracy levels.

A three-transducer reciprocity calibration method is considered for measurement of the transmitting voltage response and the free-field open-circuit receiving voltage sensitivity of a transducer radiating in air at 1 atm. Piezoelectric ceramic disks are used as the transmitting and receiving transducers, to simplify finite element (FE) analysis of the measurement setup and the measured magnitude and phase responses. Simulations are used

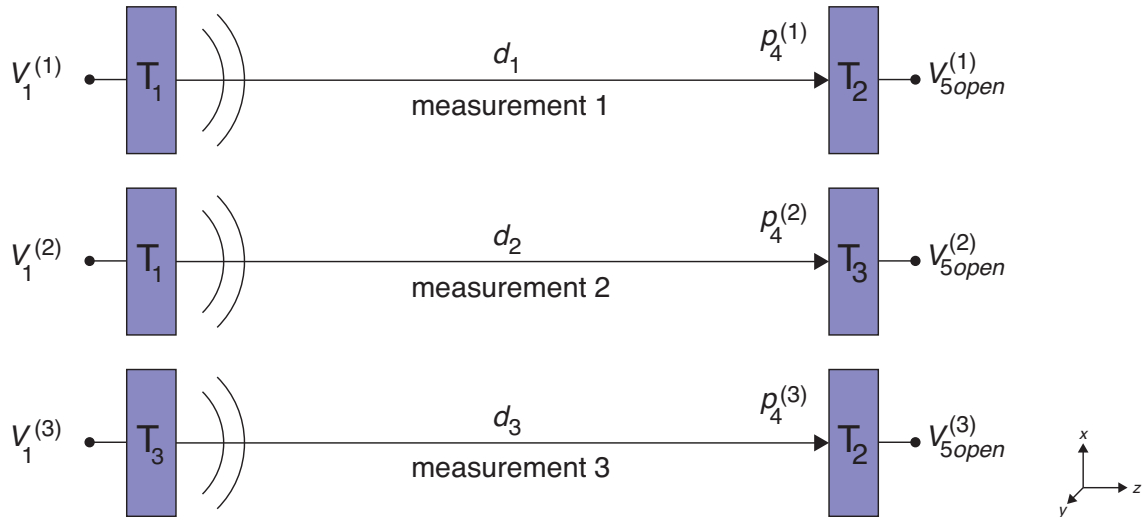


Figure 1: Schematic of the three measurements needed to perform calibration by the reciprocity calibration method.

(i) to aid in control and improvement of the measurements, (ii) for comparison with and interpretation of the measurement results, (iii) to calculate necessary correction factors to the measurements, and (iv) to determine a 360° ambiguity in the measured phase response at low frequencies, at which poor signal-to-noise ratio (SNR) is experienced.

Preliminary measurement and simulation results are shown for the magnitude and phase responses of (i) the open-circuit loss-free transmit-receive voltage-to-voltage transfer function, (ii) the transmitting voltage response, and (iii) the free-field open-circuit receiving voltage sensitivity, for circular piezoelectric ceramic disks vibrating at frequencies up to 300 kHz, a frequency band covering the first and second radial mode of the disk. Promising characterization results are obtained in the frequency range 75–125 kHz around the first radial mode at about 100 kHz, in which a SNR beyond 40 dB is achieved.

The present paper represents an update from [28], based on the work in [29], and building on prior work such as refs. [30–37].

2 Measurement theory

2.1 Reciprocity calibration method

To perform calibration by the reciprocity method three transducers and three measurements are needed, cf. Fig. 1 where T_1 acts as a transmitter, T_2 acts as a receiver, T_3 acts as a reciprocal transducer^{1, 2}, p_4 is the on-axis free- and far-field sound pressure, V_1 is the input voltage at the terminals of the transmitter, V_{5open} is the open-circuit output voltage at the terminals of the receiver, and d_1 , d_2 and d_3 are the separation distances between the transmitter and receiver for measurement 1, 2, and 3, respectively. A superscript is imposed on the quantities V_1 , p_4 and V_{5open} to denote what measurement the quantity is obtained from, and the subscripts refer to where the quantities exist in the measurement model, cf. Fig. 2.

¹ T_3 is a passive, linear and reversible electromechanical or electroacoustical transducer such that coupling is equal in either direction [38]

²It is assumed that the receivers are in the far-field of the transmitting transducer.

From the measurement set-up in Fig. 1, T_1 can be calibrated as a transmitter of sound, and T_2 can be calibrated as a receiver of sound, i.e. the calibrated quantities are the complex transmitting voltage response [7–9, 34]³

$$S_V^{T_1} = \left[\frac{1}{J^{(3)} Z_{T_3}} \frac{H_{15open}^{VV(1)} H_{15open}^{VV(2)}}{H_{15open}^{VV(3)}} \frac{d_1 d_2}{d_0 d_3} e^{-ik^{(1)}(d_0-d_1)} e^{-ik^{(2)}(d_0-d_2)} e^{ik^{(3)}(d_0-d_3)} \right]^{\frac{1}{2}}, \quad (1)$$

and the complex receiving voltage sensitivity [7–9, 34]

$$M_V^{T_2} = \left[J^{(3)} Z_{T_3} \frac{H_{15open}^{VV(1)} H_{15open}^{VV(3)}}{H_{15open}^{VV(2)}} \frac{d_1 d_3}{d_0 d_2} e^{-ik^{(1)}(d_0-d_1)} e^{ik^{(2)}(d_0-d_2)} e^{-ik^{(3)}(d_0-d_3)} \right]^{\frac{1}{2}}, \quad (2)$$

where $J^{(3)}$ is the spherical reciprocity parameter for measurement 3, Z_{T_3} is the electrical input impedance of the reciprocal transducer T_3 , $k^{(n)} = 2\pi f/c$ is the wave number for the n 'th measurement, f is frequency, c is the speed of sound, and

$$H_{5open}^{VV(n)} \equiv \frac{V_{15open}^{(n)}}{V_1^{(n)}}, \quad (3)$$

is the complex open-circuit loss-free voltage-to-voltage transfer function relating the input voltage at the transmitter to the open-circuit output voltage at the receiver for the n 'th measurement, and $n = 1, 2$ or 3 denotes the measurement number.

2.2 Open-circuit loss-free voltage-to-voltage transfer function

To perform the three measurements in Fig. 1 additional measurement equipment is needed. In Fig. 2 a schematic of the complete measurement set-up is given. Each block represents the physical equipment, or the environment, used to conduct the measurements, and in Appendix B.1, Table 1 a description of the node voltages are given.

The signal propagation is in two branches. In branch (1) the function generator [39] is connected to the transmitter through the coaxial cable 1 (RG-178), the transmitter is connected to the receiver through the medium (air), the receiver is connected to the signal amplifier [40] and filter [41] through the coaxial cable 3 (RG-178), the signal amplifier and filter are connected to the oscilloscope [42] through the coaxial cable 4 (RG-58). In branch (2) the function generator is connected to the oscilloscope through the coaxial cable 2 (RG-58).

The oscilloscope is used to record the two signals corresponding to the two branches. The recorded signals, hereby referred to as voltages, are denoted $V_{0m} = |V_{0m}|e^{i\theta_{0m}}$ and $V_6 = |V_6|e^{i\theta_6}$, where $||$ denotes magnitude, and θ_{0m} and θ_6 are the phases of V_{0m} and V_6 , respectively.

The two recorded voltages are not included in Eqs. (1) and (2), however H_{15open}^{VV} is. To obtain H_{15open}^{VV} corrections are applied to the recorded voltages. The corrections account for the influence the measurement equipment and connecting cables have on the signal propagating through the measurement set-up, and are given as transfer functions. To compensate for propagation losses in air and possible deviations from far-field conditions and near-field effects, two additional corrections are introduced, C_α and C_{dif} , respectively.

³Confer Appendix A for derivation of Eqs. (1) and (2).

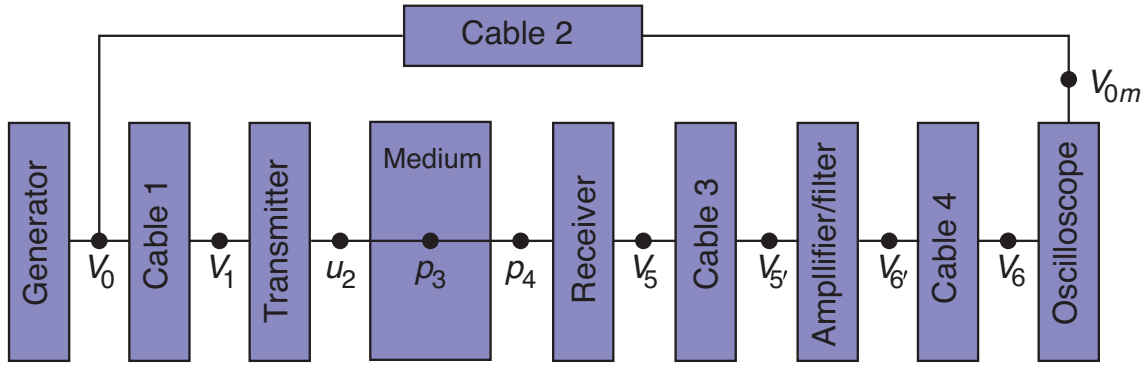


Figure 2: Model of the measurement set-up with node numbering.

A detailed description of the corrections are beyond the scope of this paper, and it is referred to e.g. [29, 31, 34, 36]. For completeness, the definitions of the corrections are given in Appendix B.2 Table 2.

When the corrections are applied to the recorded voltages the complex open-circuit loss-free transfer function is given as

$$H_{15open}^{VV} = \frac{V_6}{V_{0m}} \cdot \frac{1}{H_{0m1}^{VV} \cdot H_{5open5'}^{VV} \cdot H_{5'6open}^{VV} \cdot H_{6open6}^{VV}} \cdot C_\alpha \cdot C_{dif}, \quad (4)$$

which can be represented as

$$H_{15open}^{VV} = |H_{15open}^{VV}| e^{i\theta_{15open}}, \quad (5)$$

where $|H_{15open}^{VV}|$ is the magnitude and θ_{15open} is the phase of H_{15open}^{VV} , respectively.

The magnitude and phase of the corrections will not be discussed further, however both the phase and magnitude of the recorded voltages are the subjects of the next section, and the total expression for the phase θ_{15open} is deferred to Sec. 2.4.

2.3 Phase and magnitude of the recorded voltages V_{0m} and V_6

The function generator in Fig. 2 outputs a single frequency sinusoidal burst which length is assumed long enough for steady-state conditions to be realized at the receiver. Both V_{0m} and V_6 are recorded in the time-domain and a transformation to the frequency-domain is performed using a Fast Fourier Transform (FFT) [43]. Any transformation as such is associated with a window function, and a rectangular window, denoted FFT-window, is used in the current work. Thus, a lower and upper bound must be defined for both magnitude and phase for both voltages.

To obtain the magnitudes $|V_{0m}|$ and $|V_6|$ a steady-state region is located in the received bursts and the FFT-window's lower and upper bounds are placed in a zero crossing. The spectra are computed and only the magnitudes of the spectra are kept.

The phase of V_{0m} is obtained by placing the FFT-window's lower bound in $t = 0$, where t is time, and the upper bound in the steady-state region, towards the end of the burst. The spectrum is computed and only the phase θ_{0m} is kept.

To obtain the phase of V_6 it is useful to decompose the total phase, θ_6 , in two components: 1) the phase associated with the measurement equipment and transducers, denoted

slowly-varying phase, θ_6^{slow} , and 2) the phase associated with the acoustical wave propagation in the medium, $2\pi ft_p$. Formally, this can be stated as [43]

$$\theta_6 = \theta_6^{slow} - 2\pi ft_p, \quad (6)$$

where f is frequency, and t_p is the time-of-flight of the acoustical wave propagation in air. An estimate of t_p is obtained by

$$t_p = \frac{d}{c(f)}, \quad (7)$$

where d is the separation distance between the transmitter and receiver, and $c(f)$ is the speed of sound in air corrected for dispersion [44, 45], cf. Appendix D.

If the total phase, θ_6 , is of interest, then only an estimate of t_p is needed, i.e. t_p has to be within one signal period of the actual signal onset, cf. Appendix C. However, if the slowly-varying phase, θ_6^{slow} , is of interest, then this becomes directly dependent on t_p estimating the actual signal onset.

Estimations of t_p are associated with relatively large uncertainties due to the uncertainties in determining d , cf. Sec. 3.1, and calculating $c(f)$ ⁴. However, as an input parameter to the Eqs. (1–2) the total phase θ_{15open} is used. Thus, the total phase θ_6 is used when calculating Eqs. (1–2). The consequence of this is that the uncertainty of the phases $\angle S_V^{T1}$ and $\angle M_V^{T2}$ are not affected by the uncertainty in either d or t_p .

2.4 Phase of the open-circuit loss-free voltage-to-voltage transfer function

The phase θ_{15open} in Eq. (5) can be expressed without the exponential notation, and it can further be decomposed in a similar manner as the phase θ_6 , i.e.

$$\theta_{15open} = \theta_{15open}^{slow} - 2\pi ft_p, \quad (8)$$

where θ_{15open} is the total phase of H_{15open}^{VV} , θ_{15open}^{slow} is the slowly-varying phase associated with the transmitter and receiver⁵, and $2\pi ft_p$ is the phase associated with the acoustical wave propagation in air.

Using Eq. (4), the phases θ_{15open} and θ_{15open}^{slow} can be expressed as [29]

$$\begin{aligned} \theta_{15open} &= \theta_6 + \theta_{dif} - (\theta_{0m} + \theta_{0m1} + \theta_{5open5'} + \theta_{5'6open} + \theta_{6open6}), \\ \theta_{15open}^{slow} &= \theta_6^{slow} + \theta_{dif} - (\theta_{0m} + \theta_{0m1} + \theta_{5open5'} + \theta_{5'6open} + \theta_{6open6}), \end{aligned} \quad (9)$$

where the phases have adopted the subscript notation from Eq. (4), e.g. the phase of H_{0m1}^{VV} is denoted θ_{0m1} ⁶.

⁴Kramer [44] gives the uncertainty of the zero frequency speed of sound model to be 300 ppm. In [46] the uncertainty of the speed of sound model is indicated to be 500 ppm based on [44, 47].

⁵The phase θ_6^{slow} is associated with all of the measurement equipment, including the transmitter and receiver, however θ_{15open}^{slow} is only associated with the transmitter and receiver as corrections for the phases associated with the measurement equipment are performed.

⁶ C_α is a real quantity and does not contribute to Eq. (9).

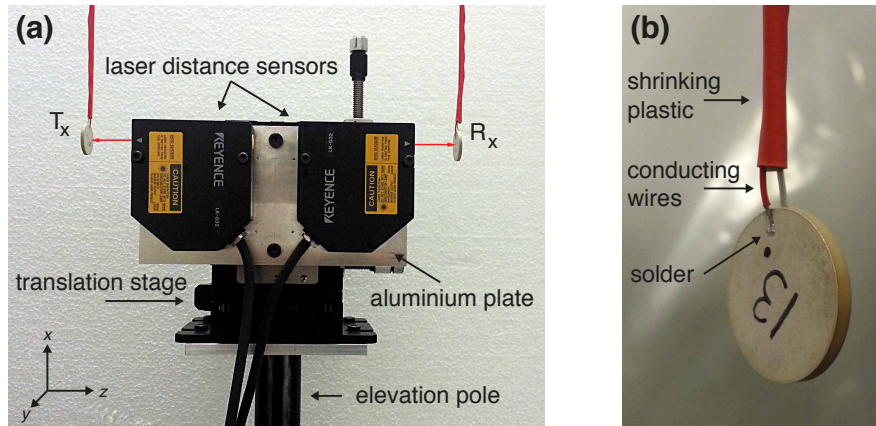


Figure 3: (a) Picture of the two laser distance sensors mounted on a manual xyz-translation stage. The laser distance sensors are shown in position for a measurement on the distance between the transmitter and receiver. (b) Picture a piezoelectric disk suspended in air.

3 Measurement methods

3.1 Measurement distance

In [29] it is shown how the separation distance between the transmitter and receiver, d , is obtained by measurements utilizing two laser distance sensors from Keyence [48], hereby referred to as sensors, and a linear translation stage LS270 from PI miCos [49]. In Fig. 3 (a) a picture of the two sensors is given ⁷. The sensors are mounted in opposite directions on a 5 mm thick aluminum plate that is mounted to a manual xyz-translation stage from Thorlabs [50]. The two sensors and the manual xyz-translation stage are moved in position for a distance measurement using an elevation pole from Gitzo [51].

When the sensors and transmitter and receiver are placed as shown in Fig. 3 (a) the separation distance between the transmitter and receiver is approximately 0.24 m. The separation distance investigated in the current work is $d = 0.50$ m. To realize a separation distance equal to 0.50 m the receiver is moved in opposite direction of the transmitter utilizing the linear translation stage. The uncertainty associated with the measurement distance, d , is calculated to be $\pm 40 \mu\text{m}$ [29].

3.2 Piezoelectric disks

In the current work piezoelectric disks from Meggit Sensing Systems ⁸ [52], of approximate diameter and thickness 20×2 mm, are used as both transmitters and receivers. In Fig. 3 (b) an picture of a piezoelectric disk suspended in air is shown. Visible in the figure are the two conducting wires (red and white) that are soldered onto the electrodes of the piezoelectric disk. The wires are fastened to a welding rod by shrinking plastic.

The consequence of this suspension method is that the alignment of the front face of the disks with the xy-plane is rather arbitrary. However, since the sensors are mounted on the xyz-translation stage, the sensors can be moved across the surface of the disks and deviations in the xy-plane can be measured. Thus, the disks can be re-aligned until

⁷The abbreviations T_X and R_X are used for transmitter and receiver, respectively.

⁸Previously known as Ferroperm.

the deviations in the xy -plane are less than a given value. In the current work the disks were re-aligned until the deviations were less than 20 μm . Re-alignment of the disks were performed by 1) loosening the screw that holds the welding rod in place and then rotating the disk, and 2) pushing on the bottom of the disk.

Measurements have indicated that failure to co-axially align the transmitter and receiver results in fluctuating phase values (not shown here).

3.3 Non-linearity in piezoelectric disks

The amplitude of the excitation voltage is 10 V, however, around the series resonance frequency (~ 100 kHz) non-linearities are observed [29, 31, 34]. The non-linearities are attributed to the transmitting piezoelectric disk. To compensate for this, a 1 V excitation voltage is used in the frequency range 90–105 kHz. Non-linearities are expected, and observed, at the second radial mode too (~ 250 kHz) [31, 34], however in the current work no compensation for this has been performed. For both the first and second radial modes the non-linearities have been observed and documented using electrical input impedance measurements [29, 31, 34].

4 Finite element modeling

All finite element simulations are performed using FEMP 5.1, Finite Element Modeling of Ultrasonic Piezoelectric Transducers [53].

For an axisymmetric simulation problem, the simulation is defined in the rz -plane, where $r = \sqrt{x^2 + y^2}$, and (x, y, z) are the Cartesian coordinates. The 3D solution is obtained by assuming symmetry about the z -axis. The simulation problem is solved using a direct harmonic analysis, with the disk immersed in a fluid. The simulation problem is divided into a region of finite elements and a region of infinite elements. The finite element region consists of the piezoelectric disk as well as the fluid loading, and is solved using 8 node isoparametric elements. The infinite element region consist of the infinite elements which are solved using 12th order conjugated Astley-Leis infinite elements. In the finite element region, seven or nine elements per shear wavelength are used in the simulations. The medium, air, is simulated without losses.

Since the material constants obtained from Ferroperm are associated with high uncertainties (as much as ± 10 percent [52]) an adjusted material data set, developed at the university of Bergen (UiB) [54], is used in the current work. However, since the material constants are not specifically adjusted for the disks used in the current work, deviations between the measurement and simulations are still expected.

5 Preliminary results and discussion

5.1 Open-circuit loss-free voltage-to-voltage transfer function, H_{15open}^{VV}

Three measurements corresponding to the measurements indicated in Fig. 1 are performed. The three measurements consist of different transmitter and receiver pairs, thus the measurement set-up has been dismantled in-between each measurement. The measurements are compared to a simulation of the same quantity.

In Fig. 4 (a) and (b) $|H_{15open}^{VV}|$ and θ_{15open}^{slow} are shown, respectively. The crosses indicate the interval where the 1 V measurements are used. The grey area, 70–125 kHz,

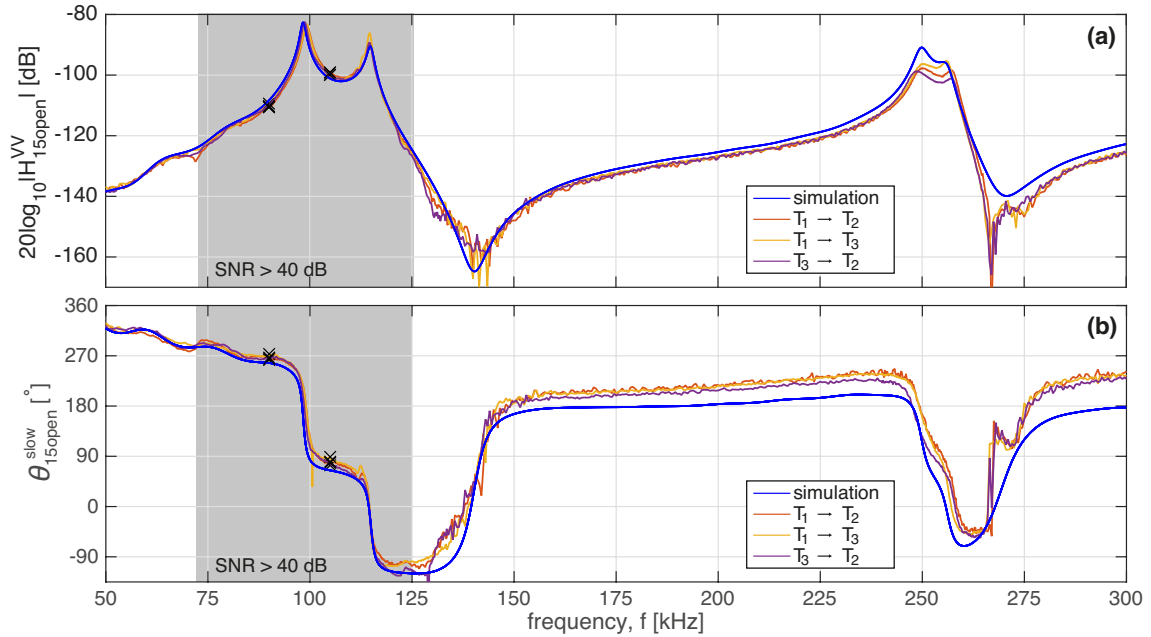


Figure 4: (a) Magnitude and (b) slowly-varying phase of the open-circuit loss-free voltage-to-voltage transfer function H_{15open}^{VV} . The grey area indicates the frequency range where a SNR > 40 dB is achieved.

indicates where a SNR > 40 dB is achieved. This frequency range corresponds to where the calibrations are expected to be performed with adequate SNR [29].

In Fig. 4 (a) around 70–125 kHz a fair correspondence between the three measurements are observed; the observed deviations are attributed to differences in the physical properties of the piezoelectric disks. A fair correspondence is also seen between the three measurements and the simulation, and the observed differences are attributed to the uncertainties in the material parameters used in the FE-simulations [29]. The deviations around 250 kHz are partly explained by non-linearities that was not compensated for by using a lower excitation voltage, and by differences in the physical properties of the piezoelectric disks. From ~160–300 kHz a frequency dependent deviation between the three measurements and the simulation is observed. It is hypothesized, but not investigated, that this deviation might partly be due to the uncertainty in the correction factor accounting for attenuation.

In Fig. 4 (b) around 70–125 kHz a fair correspondence between the three measurements are observed. A fair correspondence between the measurements and the simulations is also achieved, where the deviations are less than 20° . Above 125 kHz a frequency dependent deviation between all three measurements and the simulation is observed; at 200 kHz a deviation of $\sim 30^\circ$ is observed, and at 300 kHz a deviation of $\sim 60^\circ$ is observed. This frequency dependent deviation is hypothesized to stem from 1) deviations in the measurement distance, d , compared to the actual separation distance between the transmitter and receiver, and 2) uncertainties in the estimate t_p compared to the actual time-of-flight of the acoustical wave, and 3) deviations in the co-axial alignment of the disks with the xy -plane.

For both Fig. 4 (a) and (b) the large deviation around 260–275 kHz is attributed to diffraction effects [29].

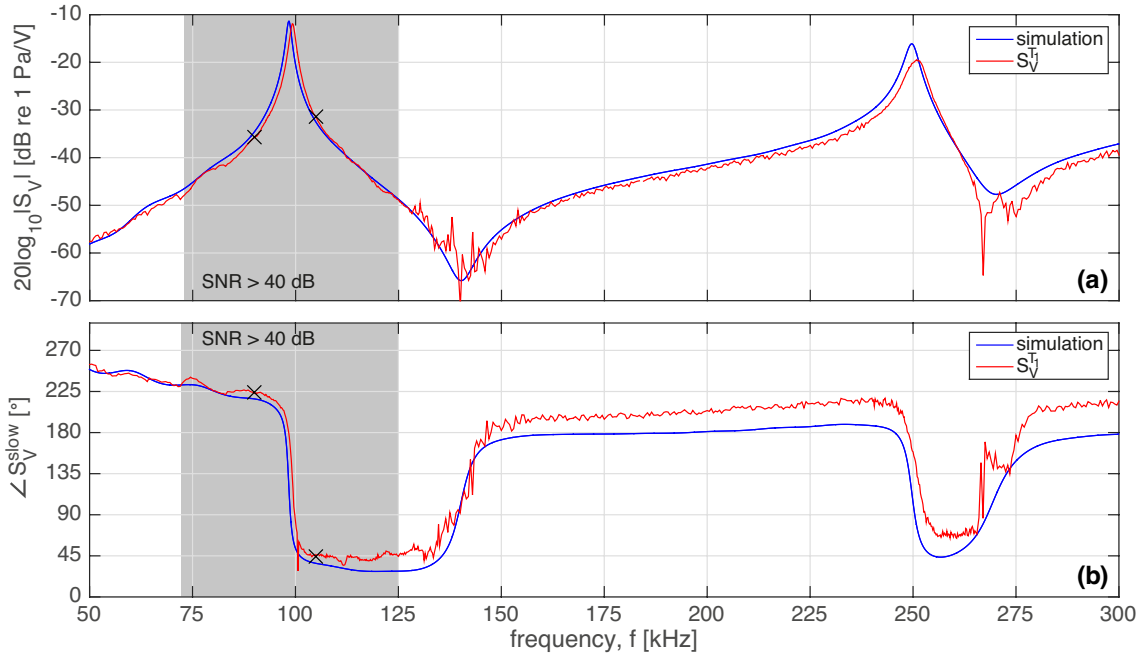


Figure 5: (a) Magnitude $|S_V|$ and (b) slowly-varying phase $\angle S_V^{slow}$ of the transmitting voltage response, S_V^{T1} . The grey area indicates the frequency range where a SNR > 40 dB is achieved.

5.2 Transmitting voltage response, S_V^{T1}

In Fig. 5 the transmitting voltage response S_V^{T1} , cf. Eq. (1), is shown for (a) magnitude $|S_V|$ and (b) slowly-varying phase $\angle S_V^{slow} = \angle S_V^{T1} + 2\pi f t_p$. The measurement is compared to a simulation of the same quantity.

In Fig. 5 (a) around 70–125 kHz a fair correspondence between the measurement and the simulation is observed. Noteworthy is the deviation around 100 kHz. The simulation peaks approximately 1 kHz before the measurement. This deviation is attributed to the material constants used in the FE-simulation⁹. The deviation around 250 kHz is partly explained by non-linearity and by the material constants used in the FE-simulations. At 200 kHz a deviation between measurement and simulations of approximately 1 dB is observed, and at 300 kHz a deviation of approximately 2 dB is observed.

In Fig. 5 (b) around 70–125 kHz a fair correspondence between the measurement and the simulation is observed, where the observed deviations are less than 10° . As in Fig. 4 (b) the deviation between the measurement and simulation increase with increasing frequency. At 200 kHz a deviation of $\sim 20^\circ$ is observed, and at 300 kHz a deviation of $\sim 35^\circ$ is observed. The deviation is hypothesized to stem from the same sources listed in Sec. 5.1.

For both Fig. 5 (a) and (b) the large deviation around 260–275 kHz is attributed to diffraction effects [29].

5.3 Receiving voltage sensitivity, M_V^{T2}

In Fig. 6 the receiving voltage response M_V^{T2} , cf. Eq. (2), is shown for (a) magnitude $|M_V|$ and (b) phase $\angle M_V$. The measurement is compared to a simulation of the same quantity.

⁹A similar deviation is observed when comparing measurements and simulations of the electrical input impedance of the piezoelectric disk (not shown here).

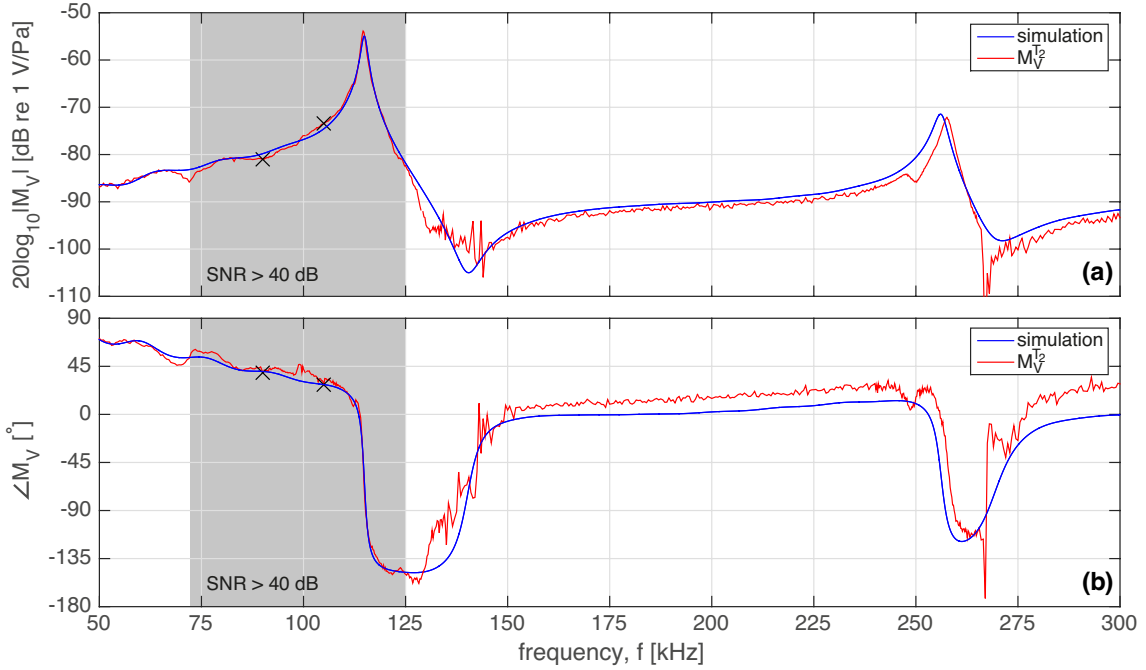


Figure 6: (a) Magnitude $|M_V|$ and (b) phase $\angle M_V$ of the receiving voltage sensitivity, $M_V^{T_2}$. The grey area indicates the frequency range where a SNR > 40 dB is achieved.

In Fig. 6 (a) around 70–125 kHz a fair correspondence between the measurement and the simulation is observed; the observed deviations are less than 2 dB. The ”dip” in the measurement at 250 kHz is due to non-linearity, and the deviation between the measurement and simulation at the peak around 255–260 kHz is partly explained by the material constants used in the FE-simulations and by non-linear effects (small). At 200 kHz the deviation between the measurement and simulation is less than 1 dB; at 300 kHz the deviation is less than 2 dB.

In Fig. 6 (b) around 70–125 kHz a fair correspondence between the measurement and the simulation is observed; the observed deviations are less than 10° . The ”dip” in the measurement at 250 kHz is due to non-linearity. As in Fig. 4 (b) and Fig. 5 (b) the deviation between the measurement and simulation increase with increasing frequency. At 200 kHz the deviation is approximately 15° ; at 300 kHz the deviation is approximately 25° . The deviation is hypothesized to stem from the same sources listed in Sec. 5.1.

For both Fig. 6 (a) and (b) the large deviation around 260–275 kHz is attributed to diffraction effects [29].

5.4 Measurement uncertainty

In Fig. 7 the estimated relative measurement uncertainties [29]

$$u_r(|M_V|) = \frac{u(|M_V|)}{|M_V|},$$

$$u_r(|H_{15open}^{VV}|) = \frac{u(|H_{15open}^{VV}|)}{|H_{15open}^{VV}|}, \quad (10)$$

are given. The red crosses indicates the interval where the 1 V excitation voltage has been used. Since $u_r(|S_V|) = u_r(|M_V|)$ this is not shown. The uncertainties are shown given a

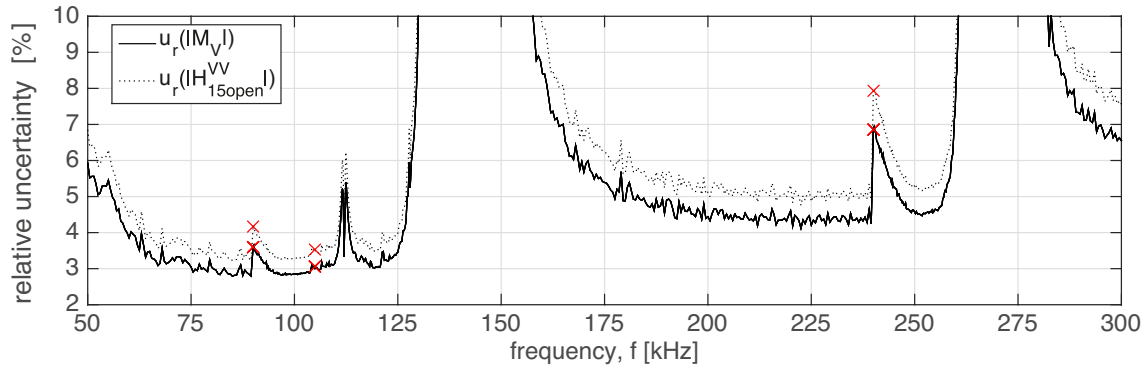


Figure 7: Relative measurement uncertainty given in percent for the magnitude of M_V and H_{15open}^{VV} .

68.3% confidence level.

Noteworthy is that the uncertainty tends to about 3% in the range 70–125 kHz. This corresponds to the measurement uncertainty of the measurement amplifier and filter (not shown here). The peak at about 112–115 kHz is due to possible lack of steady-state conditions and electromagnetic cross-talk [29]¹⁰. Above 125 kHz the large uncertainty is due to poor SNR due to low sound pressure. It is also worth noticing that $u_r(|M_V|)$ is below 5% in the range 180–240 kHz, and 245–255 kHz. This indicates that it might be possible to perform calibration with adequate SNR also in this frequency range.

A Type A uncertainty was calculated for θ_6 , and this was found to be less than 3% in the range 70–125 kHz given a 68.3% confidence level. The Type A uncertainty was obtained by 6 repeated measurements [29].

6 Conclusion

A modified conventional three-transducer reciprocity calibration method is used to characterize 20 x 2 mm circular piezoelectric ceramic disks radiating in air at 1 atm. Preliminary results are shown for the magnitude and phase responses of the transmitting voltage response and the free-field open-circuit receiving voltage sensitivity of such transducers. Frequencies up to 300 kHz are investigated, covering the first and second radial modes of the disks.

Finite element simulations of the measurement system and the measured frequency responses are used to support the measurements, interpret the results, and remove a 360° ambiguity in the measured phase response at low frequencies, at which poor signal-to-noise ratio (SNR) is experienced. A fair agreement between measured and simulated magnitude and phase responses is obtained over the frequency band up to 300 kHz.

Promising characterization results are obtained for the magnitude and phase responses in a frequency band 75–125 kHz around the first radial mode at 100 kHz, in which SNR > 40 dB is achieved.

Factors limiting the measurements include low signal-to-noise ratio (SNR) due to coherent electromagnetic noise, acoustic reflections in the measurement system, non-linearity in the piezoelectric material, and absence of true far field conditions (near field diffraction effects). A laser sensor system has been implemented and calibrated to improve

¹⁰Significant electromagnetic cross-talk is observed when the piezoelectric disks are operated with exposed electrodes.

distance measurements and transducer alignment, and thus to improve measurement reproducibility and control. A more detailed analysis and additional results can be found in [29].

Further work is needed to demonstrate and quantify the accuracy obtained using the three-transducer reciprocity calibration method, and to achieve transducer characterization at a calibration accuracy level. Further work may also address extension of the method to characterization above the calibrated frequency range of the B&K 4138 microphone. Construction of more sensitive piezoelectric transducers for gas, with reduced nonlinear effects and possibilities for improved shielding with respect to electromagnetic cross-talk, are expected to be important in these perspectives.

7 Acknowledgments

The current work is performed as part of a master project by the first author [29], supported by the Michelsen Centre for Industrial Measurement Science and Technology, Bergen, Norway.

References

- [1] “Regulations relating to measurement of petroleum for fiscal purposes and for calculation of CO₂ tax.” The Norwegian Petroleum Directorate, Stavanger, Norway (2001).
- [2] “AGA Report no. 9. Measurement of gas by ultrasonic meters. 2nd revision.” American Gas Association, Transmission Measurement Committee, Washington DC, U.S.A. (2007).
- [3] ISO 17089-1:2010, “Measurement of fluid flow in closed conduits - Ultrasonic meters for gas - Part 1: meters for custody transfer and allocation measurement.” International Organization for Standardization, Geneva, Switzerland (2010).
- [4] K.-E. Frøsa and P. Lunde, “Density and calorific value measurement in natural gas using ultrasonic flow meters,” in *Proc. 23rd International North Sea Flow Measurement Workshop*, (Tønsberg, Norway), 18-21 October 2005.
- [5] K.-E. Frøsa, P. Lunde, P. A., and J. E., “Density and calorific value measurement of natural gas using ultrasonic flow meters. results from testing on various north sea gas field data,” in *Proc. 24th International North Sea Flow Measurement Workshop*, (St. Andrews, Scotland), 24-27 October 2006.
- [6] P. Lunde, P. Norli, M. Vestrheim, and R. Kippersund, “Precision sound velocity cell as reference for gas quality measurement in ultrasonic flow meters. preliminary results using two candidate methods with argon at low pressure,” in *Proc. 30th Scandinavian Symposium on Physical Acoustics*, (Geilo, Norway), 28-31 January 2007.
- [7] ANSI/ASA S1.20-2012, “Procedures for calibration of underwater electroacoustic transducers.” American National Standards Institute, New York, 1994 (R2012).
- [8] ANSI S1.10-1976, “Method for the calibration of microphones,” American National Standards Institute, New York, 1966 (R1976).
- [9] IEC 61094-3:1995, “Measurement microphones - Part 3: Primary method for free-field calibration of laboratory standard microphones by the reciprocity technique.” International Electrotechnical Commission, Geneva, Switzerland, 1995.
- [10] L. D. Luker and A. L. Van Buren, “Phase calibration of hydrophones,” *J. Acoust. Soc. Am.*, vol. 70(2), p. 516, 1981.
- [11] G. Hayman and S. P. Robinson, “NPL Report AC 1 Phase calibration of hydrophones by the free-field reciprocity method in the frequency range 10 kHz to 400 kHz,” Tech. Rep. September, 2007.
- [12] P. L. van Neer, H. J. Vos, and N. de Jong, “Reflector-based phase calibration of ultrasound transducers,” *Ultrasonics*, vol. 51(1), pp. 1–6, 2011.
- [13] E. G. de Oliveira, R. P. B. Costa-Felix, and J. C. Machado, “Reciprocity-based method for magnitude and phase calibration of hydrophone sensitivity,” in *Ultrasonics Symposium (IUS), 2013 IEEE International*, pp. 465–468, July 2013.

- [14] I. Rudnick and M. N. Stein, "Reciprocity free field calibration of microphones to 100 kc in air," *J. Acoust. Soc. Am.*, vol. 20(6), p. 818–825, 1948.
- [15] W. Wathen-Dunn, "On the reciprocity free-field calibration of microphones," *J. Acoust. Soc. Am.*, vol. 21(5), p. 542–546, 1949.
- [16] W. Koidan, "Calibration of standard condenser microphones: Coupler versus electrostatic actuator," *J. Acoust. Soc. Am.*, vol. 44(5), p. 1451–1453, 1968.
- [17] E. Burnett and V. Nedzelnitsky, "Free-field reciprocity calibration of microphones," *Journal of Research of the National Bureau of Standards*, vol. 92(2), p. 129, 1987.
- [18] E. W. Burnett and V. Nedzelnitsky, "Free-field reciprocity calibration of microphones," in *Journal of Research of the National Bureau of Standards*, vol. 92(2), p. 129–151, 1987.
- [19] J. Hietanen and M. Oksanen, "Photoacoustic testing of ultrasonic air transducers," in *Measurement Science and Technology*, vol. 5(8), p. 960, 1994.
- [20] A. Gachagan, G. Hayward, S. Kelly, and W. Galbraith, "Characterization of air-coupled transducers," in *IEEE Trans. Ultrason., Ferroelectr., Freq. Control*, vol. 43(4), p. 678–689, 1996.
- [21] M. J. Anderson, "Use of reciprocity to characterize ultrasonic transducers in air above 100 kHz," *J. Acoust. Soc. Am.*, vol. 103(1), pp. 446–453, 1998.
- [22] W. Galbraith and G. Hayward, "Development of a PVDF membrane hydrophone for use in air-coupled ultrasonic transducer calibration," *IEEE Transactions on Ultrasonics, Ferroelectrics, and Frequency Control*, vol. 45(6), pp. 1549–1558, 1998.
- [23] O. B. Matar, L. Pizarro, D. Certon, J. Remenieras, and F. Patat, "Characterization of airborne transducers by optical tomography," *Ultrasonics*, vol. 38(1–8), p. 787 – 793, 2000.
- [24] S. Barrera-Figueroa, *New methods for transducer calibration: Free-field reciprocity calibration of condenser microphones*. PhD thesis, Technical University of Denmark, Ørsted, Denmark, 2003.
- [25] N. Bouaoua, *Free-field Reciprocity Calibration of Condenser Microphones in the Low Ultrasonic Frequency Range*. PhD thesis, Universität Oldenburg, Germany, 2008.
- [26] Brüel & Kjær, "Condenser microphones and microphone preamplifiers for acoustic measurements - Data handbook." Denmark, 2008.
- [27] Brüel & Kjær, "Calibration data for Type 4138-A-015 microphone system serial no. 2795107." Denmark, 2012.
- [28] K. K. Andersen, A. A. Søvik, P. Lunde, M. Vestrheim, and J. Kocbach, "Reciprocity calibration method for ultrasonic piezoelectric transducers in air. Comparison of finite element modelling and experimental measurements," in *Proc. 38th Scandinavian Symp. on Physical Acoust.*, Geilo, Norway, 1-4 February 2015. Norwegian Physics Soc., <http://www.norskfysikk.no>.

- [29] K. K. Andersen, "Reciprocity calibration of ultrasonic piezoelectric disk in air," Master's thesis, Department of Physics and Technology, University of Bergen, November 2015.
- [30] E. Storheim, *Diffraction effects in the ultrasonic field of transmitting and receiving circular piezoceramic disks in radial mode vibration*. PhD thesis, University of Bergen, Department of Physics and Technology, Bergen, Norway, 2015.
- [31] R. Hauge, "Finite element modeling of ultrasound measurement systems for gas. Comparison with experiments in air," Master's thesis, Department of Physics and Technology, University of Bergen, Norway, June 2013.
- [32] R. Hauge, E. N. Mosland, E. Storheim, P. Lunde, M. Vestrheim, and J. Kocbach, "Finite element modeling of ultrasound measurement systems for gas. Comparison with experiments in air," in *Proc. 36th Scandinavian Symp. on Physical Acoust.*, Geilo, Norway, 3-6 February 2013. Norwegian Physics Soc., <http://www.norskfysikk.no>.
- [33] R. Hauge, E. N. Mosland, E. Storheim, P. Lunde, M. Vestrheim, and J. Kocbach, "Updated results on finite element modeling of a transmit-receive ultrasound measurement system. Comparison with experiments in air," in *Proc. 37th Scandinavian Symp. on Physical Acoust.*, Geilo, Norway, 2-5 February 2014. Norwegian Physics Soc., <http://www.norskfysikk.no>.
- [34] E. Mosland, "Reciprocity calibration method for ultrasonic piezoelectric transducers in air," Master's thesis, Department of Physics and Technology, University of Bergen, Norway, June 2013.
- [35] E. N. Mosland, R. Hauge, E. Storheim, P. Lunde, M. Vestrheim, and J. Kocbach, "Reciprocity calibration method for ultrasonic, piezoelectric transducers in air, including finite element simulations," in *Proc. 36th Scandinavian Symp. on Physical Acoust.*, Geilo, Norway, 3-6 February 2013. Norwegian Physics Soc., <http://www.norskfysikk.no>.
- [36] A. A. Søvik, "Ultrasonic measurement system for gas. Finite element modelling compared with measurements in air," Master's thesis, Department of Physics and Technology, University of Bergen, June 2015.
- [37] A. A. Søvik, K. K. Andersen, P. Lunde, M. Vestrheim, and J. Kocbach, "Characterization of ultrasound transmit-receive measurement systems in air. Comparison of finite element modelling and experimental measurements," in *Proc. 38th Scandinavian Symp. on Physical Acoust.*, Geilo, Norway, 1-4 February 2015. Norwegian Physics Soc., <http://www.norskfysikk.no>.
- [38] ANSI S1.1-1994, "Acoustical Terminology." American National Standards Institute, New York, 1994.
- [39] Agilent technologies, Inc., Headquarters, 5301 Stevens Creek Blvd, Santa Clara, CA 95051, US, *User's guide - Agilent 33220A 20 MHz Waveform generator*, 2007.
- [40] Brüel & Kjær, "Product Data, Wide Range Measuring Amplifiers - Types 2610 and 2636," 1996.

- [41] Krohn-Hite Corporation, 15 Jonathan Drive, Unit 4, Brockton, MA 02301, *Product data - Krohn-Hite Model 3940*, 2014.
- [42] Tektronix Inc., 14150 SW Karl Braun Drive, Beaverton, OR 97077, United States, *DPO3000 Series Datasheet*, 2013.
- [43] E. O. Brigham, *The Fast Fourier Transform and its application*. Prentice-Hall International Editions, 1988.
- [44] O. Cramer, “The variation of the specific heat ratio and the speed of sound in air with temperature, pressure, humidity, and CO₂ concentration,” *J. Acoust. Soc. Am.*, vol. 93, pp. 2510–2516, 1993.
- [45] C. L. Morfey and G. P. Howell, “Speed of sound in air as a function of frequency and humidity,” *J. Acoust. Soc. Am.*, vol. 68, no. 5, pp. 1525–1527, 1980.
- [46] R. J. Jackett and R. G. Barham, “Phase sensitivity uncertainty in microphone pressure reciprocity calibration,” *Metrologia*, vol. 50, no. 2, pp. 170–179, 2013.
- [47] G. S. K. Wong, “Comments on “the variation of the specific heat ratio and the speed of sound in air with temperature, pressure, humidity, and CO₂ concentration” [J. acoust. soc. am. 93, 2510–2516 (1993)],” *The Journal of the Acoustical Society of America*, vol. 97, no. 5, pp. 3177–3179, 1995.
- [48] Keyence Corporation, 1100 North Arlington Heights Road, Suite 210, Itasca, IL 60143, United States, *LK-G Series User’s Manual*, 2010. www.keyence.com.
- [49] PI miCos GmbH, Freiburger Strasse 30, 79427 Eschbach, Germany, *SMC hydra TT 2 axes Controller System*, 2014.
- [50] 56 Sparta Avenue, Newton, NJ, United States, *Thorlabs, Inc.*
- [51] Via Valsugana 100, 36022 Cassola (VI) Italy, *Gitzo SA*.
- [52] Porthusvej 4, 3490 Kvistgård, Denmark, *Meggitt Sensing Systems*, 2013.
- [53] J. Kocbach, *Finite Element Modeling of Ultrasonic Piezoelectric Transducers*. PhD thesis, Department of Physics, University of Bergen, Norway, 2000.
- [54] V. Knappskog, “Radiellmode svingninger i piezoelektriske ultralydstransdusere for luft. Målinger og endelig element analyse,” Master’s thesis, Department of Physics and Technology, University of Bergen, 2007. (in Norwegian).
- [55] L. L. Foldy and H. Primakoff, “A General Theory of Passive Linear Electroacoustic Transducers and the Electroacoustic Reciprocity Theorem. I,” *J. Acoust. Soc. Am.*, vol. 17, no. 2, pp. 109–120, 1945.
- [56] ANSI S1.26-1995, “Method for calculation of the absorption of sound by the atmosphere,” American National Standards Institute, New York, 1995.
- [57] M. Vestrheim, “Phys373 - Akustiske målesystem.” Lecture notes, Department of Physics and Technology, University of Bergen, Norway (in Norwegian), 2013.

Appendix A Derivation of the reciprocity calibration equations

In the current section the derivation of $M_V^{T_2}$ and $S_V^{T_1}$ will be presented. These equations will be referred to as the reciprocity calibration equations. The derivations are based upon [34], which are similar to the equations used in e.g. [7]. The derivation in this section differ from both due to the wave number $k = 2\pi f/c$, where c is the speed of sound. The speed of sound is dependent on several environmental parameters: temperature, relative humidity, ambient pressure and CO₂ concentration [44]. The calibration by the reciprocity method utilizes three measurements where each measurement is associated with a k . In general, the three k 's will differ in value. Incorrect handling of the three k 's might therefore lead to wrong phase values.

A.1 Receiving voltage sensitivity, M_V

From Fig. 1 three voltage-to-voltage transfer functions, H_{15open}^{VV} , are identified:

$$H_{15open}^{VV(1)} \equiv \frac{V_{5open}^{(1)}}{V_1^{(1)}} = M_V^{T_2(1)} S_V^{T_1(1)} \frac{d_0}{d_1} e^{ik^{(1)}(d_0-d_1)}, \quad (11)$$

$$H_{15open}^{VV(2)} \equiv \frac{V_{5open}^{(2)}}{V_1^{(2)}} = M_V^{T_3(2)} S_V^{T_1(2)} \frac{d_0}{d_2} e^{ik^{(2)}(d_0-d_2)}, \quad (12)$$

$$H_{15open}^{VV(3)} \equiv \frac{V_{5open}^{(3)}}{V_1^{(3)}} = M_V^{T_2(3)} S_V^{T_3(3)} \frac{d_0}{d_3} e^{ik^{(2)}(d_0-d_3)} \quad (13)$$

where the superscripts refer to what measurements the transfer functions are obtained from. Dividing Eq. (11) on (12) and solving for $M_V^{T_2(1)}$ yields

$$M_V^{T_2(1)} = M_V^{T_3(2)} \frac{H_{15open}^{VV(1)} d_1}{H_{15open}^{VV(2)} d_2} e^{-ik^{(1)}(d_0-d_1)} e^{ik^{(2)}(d_0-d_2)}. \quad (14)$$

The spherical reciprocity parameter, J , is defined as the ratio of receiving voltage sensitivity to the transmitting current response [55], i.e.:

$$J \equiv \frac{M_V}{S_I} = \frac{M_V}{S_V Z_T}, \quad (15)$$

where Z_T is the impedance of the transmitting transducer. Solving Eq. (15) for S_V while applying correct notation, yields

$$S_V^{T_3(3)} = \frac{M_V^{T_3(3)}}{J^{(3)} Z_{T_3}}, \quad (16)$$

where the quantities adopt the environmental dependencies from measurement three since $S_V^{T_3(3)}$ in Eq. (16) will replace $S_V^{T_3(3)}$ in Eq. (13), i.e.:

$$H_{15open}^{VV(3)} = M_V^{T_2(3)} \frac{M_V^{T_3(3)}}{J^{(3)} Z_{T_3}} \frac{d_0}{d_3} e^{ik(d_0-d_3)}. \quad (17)$$

Solving Eq. (17) for $M_V^{T_3(3)}$, inserting the result in Eq. (14) and solving for $M_V^{T_2}$, yields

$$M_V^{T_2} = \left[J^{(3)} Z_{T_3} \frac{H_{15open}^{VV(1)} H_{15open}^{VV(3)}}{H_{15open}^{VV(2)}} \frac{d_1 d_3}{d_0 d_2} e^{-ik^{(1)}(d_0-d_1)} e^{ik^{(2)}(d_0-d_2)} e^{-ik^{(3)}(d_0-d_3)} \right]^{\frac{1}{2}}. \quad (18)$$

A.2 Transmitting voltage response, S_V

Dividing Eq. (11) on (13) and solving for $S_V^{T_1(1)}$ yields

$$S_V^{T_1(1)} = S_V^{T_3(3)} \frac{H_{15open}^{VV(1)}}{H_{15open}^{VV(3)}} \frac{d_1}{d_3} e^{-ik^{(1)}(d_0-d_1)} e^{ik^{(3)}(d_0-d_3)}. \quad (19)$$

Use of Eq. (16) to replace $S_V^{T_3(3)}$ in Eq. (19), yields

$$S_V^{T_1(1)} = \frac{M_V^{T_3(3)}}{J^{(3)} Z_{T_3}} \frac{H_{15open}^{VV(1)}}{H_{15open}^{VV(3)}} \frac{d_1}{d_3} e^{-ik^{(1)}(d_0-d_1)} e^{ik^{(3)}(d_0-d_3)}. \quad (20)$$

Solving Eq. (12) with respect to $M_V^{T_3(2)}$, inserting the result in Eq. (20) and solving for $S_V^{T_1}$ yields

$$S_V^{T_1} = \left[\frac{1}{J^{(3)} Z_{T_3}} \frac{H_{15open}^{VV(1)} H_{15open}^{VV(2)}}{H_{15open}^{VV(3)}} \frac{d_1 d_2}{d_0 d_3} e^{-ik^{(1)}(d_0-d_1)} e^{-ik^{(2)}(d_0-d_2)} e^{ik^{(3)}(d_0-d_3)} \right]^{\frac{1}{2}}. \quad (21)$$

Appendix B Measurement set-up

B.1 Electromechanical quantities of the measurement set-up

Table 1: Electromechanical quantities of the measurement set-up.

Quantity	Description
$V_0 = V_0(f)$	output voltage at the terminals of the function generator
$V_{0m} = V_{0m}(f)$	recorded voltage given the signal transmission through cable 2
$V_1 = V_1(f)$	input voltage at the terminals of the transmitting disk
$u_2(r = 0, f)$	particle displacement at the center of the face of the transmitting disk
$p_3 = p_3(d_0, f)$	on-axis free- and far-field sound pressure at a ref. distance $d_0 = 1$ m
$p_4 = p_4(r, d, f)$	free-field sound pressure at a separation distance $z = d$
$V_5 = V_5(f)$	output voltage at the terminals of the receiving disk
$V_{5'} = V_{5'}(f)$	input voltage at the terminals of the amplifier
$V_{6'} = V_{6'}(f)$	output voltage at the terminals of the amplifier
$V_6 = V_6(f)$	input voltage at the terminals of the oscilloscope
Quantities not readily visible in Fig. 2	
$V_{5open} = V_{5open}(f)$	open-circuit output voltage at the terminals of the receiving disk
$V_{6open} = V_{6open}(f)$	open-circuit output voltage at the terminals of the amplifier
$V_{gen} = V_{gen}(f)$	open-circuit generator voltage

In Table 1 (r, z) are the coordinates in a cylindrical coordinate system ¹¹, where $r = \sqrt{x^2 + y^2}$, and (x, y, z) are the Cartesian coordinate axes.

B.2 Corrections

Table 2: Corrections used in Eq. (4).

Quantity	Correction accounting for:	Estimation method
$H_{0m1}^{VV} \equiv \frac{V_1}{V_{0m}}$	Oscilloscope input impedance, cable 1, cable 2, and transmitter electrical impedance	Transmission line model calculation, measurement of transmitter input electrical impedance
$H_{5open5'}^{VV} \equiv \frac{V_{5'}}{V_{5open}}$	Receiver electrical impedance, cable 3 and amplifier input impedance	Transmission line model calculation, measurement of receiver input electrical impedance
$H_{5'6open}^{VV} \equiv \frac{V_{6open}}{V_{5'}}$	Amplifier and filter	Measurement
$H_{6open6}^{VV} \equiv \frac{V_6}{V_{6open}}$	Amplifier output impedance, cable 4 and oscilloscope input impedance	Transmission line model calculation
C_α	Attenuation	Calculation by ANSI S1.26 [56]
C_{dif}	Diffraction	FE-simulation

Appendix C Phase of a time-shifted Fourier transform signal

In Fig. 8 a schematic of a sinusoidal signal, $V_6(t)$ ¹², that is time-shifted with a constant t_0 is given. In the same figure, a FFT-window is indicated, where the lower bounds of the FFT-window is placed in t_p . A discrepancy between the actual onset of the time-shifted signal and the position of the FFT-window's lower bound is seen. This time-discrepancy is denoted $\Delta t = t_0 - t_p$. Two examples will be presented: 1) $\Delta t = 0$, and 2) $\Delta t > 0$. The first example illustrates the phase contributions given that the FFT-window's lower bound is placed in the actual signal onset, whereas the second example illustrates why the FFT-window's lower bound has to be placed within one signal period of the actual signal onset.

The case where $\Delta t = 0$ will be considered first. In [43] it is shown that the Fourier transform of a time-shifted signal, $V_6(t - t_p)$, can be solved substituting $s = t - t_p$, i.e.

¹¹Note that due to the axisymmetry of the system the azimuthal (θ) is suppressed from the cylindrical coordinates, (r, θ, z) .

¹²The notation V_6 will be used in the examples in the current section, however the examples that will be given are of a time-shifted sinusoid, i.e. no phase distortions in e.g. a transmitter or receiver exist.

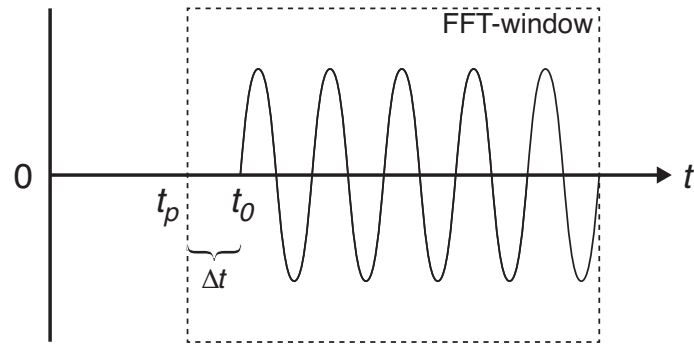


Figure 8: Schematic of a sinusoidal signal time-shifted with a constant t_0 . The FFT-window's lower bound is placed in t_p .

$$\begin{aligned}
 \int_{-\infty}^{\infty} V_6(t - t_p) e^{-i2\pi ft} dt &= \int_{-\infty}^{\infty} V_6(s) e^{-i2\pi f(s+t_p)} ds \\
 &= e^{-i2\pi ft_p} \int_{-\infty}^{\infty} V_6(s) e^{-i2\pi fs} ds \\
 &= e^{-i2\pi ft_p} V_6(f) \\
 &= |V_6(f)| e^{i(\theta_6^{slow} - 2\pi ft_p)}
 \end{aligned} \tag{22}$$

where $2\pi ft_p$ is a linear phase dependent on frequency, f , and the time-shift constant t_p , and θ_6^{slow} is the phase of the sine wave. The phases can be expressed without the exponential notation as

$$\begin{aligned}
 \theta_6 &= \theta_6^{slow} - 2\pi ft_p \\
 &= \theta_6^{slow} - 2\pi ft_0,
 \end{aligned} \tag{23}$$

since $t_p = t_0$. In the current example only a time-shifted sine wave is considered. However, if a signal is propagating through physical measurement equipment phase distortions will generally occur in the equipment. These phase distortions will then be associated with θ_6^{slow} since the position of the FFT-window remains the same.

The case where $\Delta t > 0$ will now be considered. The time-shifted signal can now be expressed as $V(t - t_p - \Delta t)$, and $s = t - t_p - \Delta t$. The derivation will be omitted, but the phases can be expressed as:

$$\begin{aligned}
 \theta_6 &= \theta_6^{slow} - 2\pi f(t_p + \Delta t) \\
 &= \theta_6^{slow} - 2\pi ft_0,
 \end{aligned} \tag{24}$$

which is the same results as in Eq. (23). That is, the phase θ_6 is independent of the placement of the FFT-window as long as $\Delta t < T$, where $T = 1/f$ is signal period. If $\Delta t > T$ phase offsets equal to $N \cdot 2\pi$, where N is an integer, will occur. To understand this one needs to remember that the phase values of a Fourier transform are confined to $\pm\pi$, and recollect that both phases θ_6^{slow} and $2\pi f\Delta t$ are obtained by the Fourier transform. Formally this can be stated as

$$-\pi \leq \angle e^{i(\theta_6^{slow} - 2\pi f\Delta t)} \leq \pi, \tag{25}$$

where \angle denotes the phase angle.

Appendix D Equations for the speed of sound

The sound speed model proposed by Cramer takes into account the temperature in Kelvin, T_K , atmospheric pressure, p , humidity and CO₂ concentration, and is given in [44] as

$$c_0^2 = \gamma \frac{RT_K}{M} \left(1 + \frac{2pB}{RT_K} \right), \quad (26)$$

where c_0 is the zero frequency speed of sound, $\gamma = C_P/C_V$ is the specific heat ratio where C_P and C_V are the specific heat at constant pressure and volume, respectively, R is the universal gas constant, M is the molecular mass and B is the second virial coefficient of state.

The expression in Eq. (26) can be expanded to account for dispersion due to the vibrational relaxation effects of oxygen and nitrogen, both of which are functions of frequency and are regarded as the greatest contributors to the absorption of sound by the atmosphere [57]. The speed of sound can then be estimated using a model, proposed by Morfey and Howell [45], which takes into account dispersion:

$$\frac{1}{c_0} - \frac{1}{c} = \frac{\alpha_{vN}}{2\pi f_{rN}} + \frac{\alpha_{vO}}{2\pi f_{rO}}, \quad (27)$$

where $c = c(f)$ is the estimated speed of sound at a frequency f including effects of dispersion, α_{vN} and α_{vO} are the plane wave attenuation coefficients due to vibrational relaxation of nitrogen and oxygen, respectively, and f_{rN} and f_{rO} are the relaxation frequencies for nitrogen and oxygen, respectively.